Wind and Structures, Vol. 5, No. 2~4 (2002) 209-226
DOI: http://dx.doi.org/10.12989/was.2002.5.2_4.209

Generation of inflow turbulent boundary layer for LES computation

K. Kondo† and M. Tsuchiya‡

Kajima Technical Research Institute, 2-19-1, Tobitakyu, Chofu-shi, Tokyo 182-0036, Japan

A. Mochida‡†

Graduate School of Engineering, Tohoku Univ., Aoba 06, Sendai 980-8579, Japan

S. Murakami‡‡

Keio University, 3-14-1 Hiyoshi, Kohoku-ku, Yokohama 223-8522, Japan

Abstract. When predicting unsteady flow and pressure fields around a structure in a turbulent boundary layer by Large Eddy Simulation (LES), velocity fluctuations of turbulence (inflow turbulence), which reproduce statistical characteristics of the turbulent boundary layer, must be given at the inflow boundary. However, research has just started on development of a method for generating inflow turbulence that satisfies the prescribed turbulence statistics, and many issues still remain to be resolved. In our previous study, we proposed a method for generating inflow turbulence and confirmed its applicability by LES of an isotropic turbulence. In this study, the generation method was applied to a turbulent boundary layer developed over a flat plate, and the reproducibility of turbulence statistics predicted by LES computation was examined. Statistical characteristics of a turbulent boundary layer developed over a flat plate were investigated by a wind tunnel test for modeling the cross-spectral density matrix for use as targets of inflow turbulence generation for LES computation. Furthermore, we investigated how the degree of correspondence of the cross-spectral density matrix of the generated inflow turbulence with the target cross-spectral density matrix estimated by the wind tunnel test influenced the LES results for the turbulent boundary layer. The results of this study confirmed that the reproduction of cross-spectra of the normal components of the inflow turbulence generation is very important in reproducing power spectra, spatial correlation and turbulence statistics of wind velocity in LES.

Key words: LES; inflow turbulence; turbulent boundary layer; cross-spectral density matrix.

1. Introduction

In designing a structure, it is necessary to investigate a wide range of phenomena, such as wind environment, wind loads on cladding and structural frame, habitability under wind-induced

† Chief Research Engineer, Dr. Eng.
‡ Senior Research Engineer
‡† Associate Professor, Dr. Eng.
‡‡ Professor, Dr. Eng.

vibration, aerodynamic instability, and fatigue damage to structural frame members. We must examine the characteristics of the flowfield around the structure and the pressure distribution on its surfaces. In recent years, Computational Fluid Dynamics (CFD) have been applied to investigate unsteady flow and pressure fields around a structure. However, care is needed in applying this method to prediction of fluctuating wind loads or structural vibrations, because the accuracy of its results has not been confirmed. This is attributed to the followings; (i) the flowfield around a structure is very complicated including such as a separated flow and a vortex shedding, (ii) the Reynolds number is very high, and (iii) the approaching flow is a turbulent boundary layer. One of the most potentially useful methods to resolve these issues and to put CFD to practical use is Large Eddy Simulation (LES), which introduces concepts of filtering in computational grids. When we predict the flowfield around a structure by unsteady computation using LES, it is important to use a reliable method of reproducing statistical characteristics of the turbulent boundary layer at the inflow boundary. This is because the statistical characteristics of the approaching flow, such as mean velocity profile, turbulence intensity, turbulence scale, power spectral density and spatial correlation, strongly influence the characteristics of the temporally and spatially fluctuating velocity field around the structure and the fluctuating pressure distribution on its surfaces. However, research has just started on development of a method for generating spatially distributed velocity fluctuations that satisfy the prescribed turbulence statistics, and many issues remain to be resolved. With this in mind, the author has undertaken research into a method of generating velocity fluctuations for the inflow boundary condition (inflow turbulence) of CFD.

The methods of generating inflow turbulence can be classified the following two groups.

(1) Computing turbulent flowfield by CFD
(2) Artificially simulating time series of velocity fluctuations by generating random numbers

The former method (1) is to conduct a preliminary computation of a temporally or spatially developing turbulent boundary layer (Lund, Wu and Squires 1998), such as a channel flow, an atmospheric boundary layer flow, etc. using LES or Direct Numerical Simulation (DNS), or to generate the turbulent flow by turbulence grids or turbulence blocks set at the inflow boundary of the computational domain of LES or DNS. These methods have advantages that the turbulent flow generated in the computational process satisfies the Navier-Stokes (N-S) equations and the continuity equation, and simulates the instantaneous coherent structure, as the turbulent boundary layer is developed by CFD. Therefore, when velocity fluctuations generated by the method (1) are given as the inflow boundary condition for LES of flow around a structure, the N-S equations and the continuity equation are satisfied without transition of the statistical characteristics and the coherent structure. However, these methods require a large computational load and the turbulence statistics from the preliminary computations are not guaranteed to correspond to the prescribed target turbulence statistics.

The latter method (2) can be classified into two groups. One uses the 3-D energy spectrum in the wave number domain obtained from spatial correlation of velocity fluctuations as the target (Iizuka, Murakami, Tsuchiya and Mochida 1999). This method has the advantage that the continuity condition can be imposed on the generation procedure. Furthermore, the time series of velocity fluctuations need not be stored, since inflow turbulence is generated at each time step of the LES. Thus, the computer memory required for this method is usually less than that for the method described below. In the boundary layer flow, however, it is hard to prescribe the 3-D energy spectrum as the target. This is a very serious disadvantage of this method from the viewpoint of application to Computational

Wind Engineering (CWE). The other group uses power spectral density and cross-spectral density in the frequency domain obtained from the time series of velocity fluctuations at the same point or two different points (Kondo, Mochida and Murakami 1997, Maruyama, Rodi, Maruyama and Hiraoka 1999). Compared with the 3-D energy spectrum, these frequency spectra can be relatively easily defined as targets from measured data of boundary layer flow. This is a very important advantage of the latter method based on frequency spectra over the former method utilizing the 3-D energy spectrum in the wave number domain. However, the continuity condition cannot be imposed on the generation procedure with this method. Therefore, divergence-free operation is indispensable in making inflow turbulence satisfy the continuity equation after the generation procedure. Furthermore, a step-by-step generation method considering conditioned probability density should be employed since the inflow turbulence cannot be generated at all grid points simultaneously. Taking the advantages and disadvantages of these methods into consideration, we employed the latter.

Modeling of the target cross-spectral density matrix, which is considered as the target at inflow turbulence generation, is indispensable for this generation method. For this purpose, fundamental turbulence statistics of a turbulent boundary layer developed over a flat plate were measured in a wind tunnel test. We proposed detailed model equations of power spectral density and cross-spectral density, considering the influence of the wind tunnel floor. We also investigated how the degree of correspondence of the cross-spectral density matrix of the generated inflow turbulence with the target cross-spectral density matrix influenced the LES results of a turbulent boundary layer. Some types of inflow turbulence were generated by this method, considering several reproduction levels of target cross-spectral density matrices, and LES was conducted using the above types of inflow turbulence.

2. Wind tunnel test of turbulent boundary layer developed over flat plate

Statistical characteristics of a turbulent boundary layer developed over a flat plate were investigated by a wind tunnel test to model a cross-spectral density matrix for use as targets of inflow turbulence generation. The Göttingen type boundary layer wind tunnel belonging to the Kajima Technical Research Institute was used for the wind tunnel test. Fig. 1 outlines of the wind tunnel test. The length scale and the time scale were normalized by the boundary layer height $L_b = 0.35$ m at the inflow boundary ($x_1 = 0$) and the mean velocity $U_b = 14.5$ m/s at that height. The Reynolds number ($= U_b L_b/\nu$) was 3.4×10^5. The wind velocity was measured by an X-type hot-wire anemometer

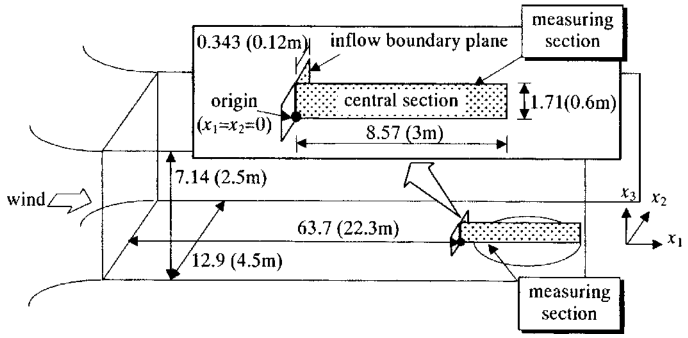

Fig. 1 Outline of wind tunnel test (Length is normalized by boundary layer height $L_b = 0.35$ m)

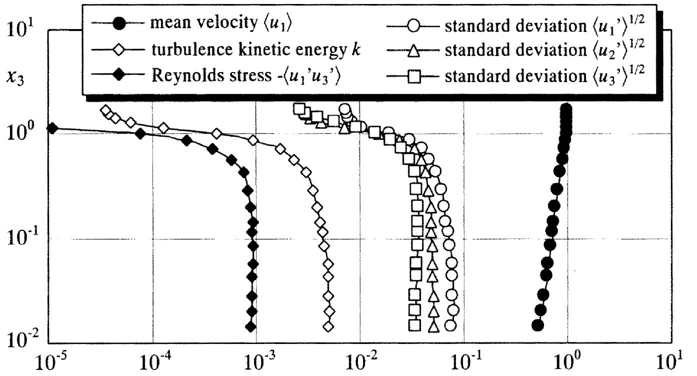

Fig. 2 Vertical profiles of turbulence statistics measured by wind tunnel test

(DANTEC 55P51) installed on a traversing device. Another X-type hot-wire anemometer was installed to measure the spatial correlation between two different points on the inflow boundary plane.

Fig. 2 shows vertical profiles of turbulence statistics for a mean velocity $\langle u_1 \rangle$, rms velocities $\langle u_1'^2 \rangle^{1/2}$, $\langle u_2'^2 \rangle^{1/2}$, $\langle u_3'^2 \rangle^{1/2}$, a turbulence kinetic energy k and a Reynolds stress $-\langle u_1' u_3' \rangle$ at $x_1 = x_2 = 0$. Here, $\langle \rangle$ means the time averaging. The power law component of the vertical profile of the mean velocity $\langle u_1 \rangle$ is about 1/7. The ratio of the variance of each fluctuating velocity near the floor is $\langle u_1'^2 \rangle$: $\langle u_2'^2 \rangle$:$\langle u_3'^2 \rangle$ = 1.0 : 0.46 : 0.19.

When the inflow turbulence is generated by our method, Fourier coefficients of velocity fluctuations are simulated by Monte Carlo simulation using a trigonometric series with Gaussian random coefficients. This is because the frequency distribution of the time series of velocity fluctuation can be regarded as a Gaussian distribution. Fig. 3 shows vertical profiles of skewness and flatness factor of each velocity component. The skewness and flatness at height $x_3 \leq 0.6$ are nearly a Gaussian distribution (skewness = 0.0, flatness = 3.0). At the height of $x_3 \geq 0.6$, the differences between those measured values and Gaussian distribution gradually increase. However, since the amplitudes of velocity fluctuations are small near the boundary layer height, we assume that the frequency

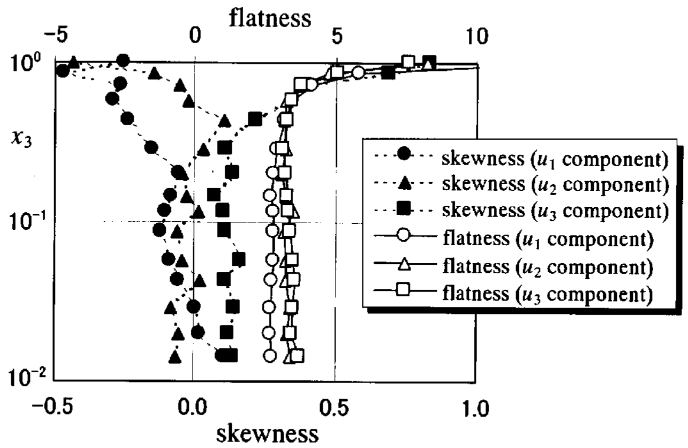

Fig. 3 Vertical profiles of skewness and flatness factor of velocity fluctuations

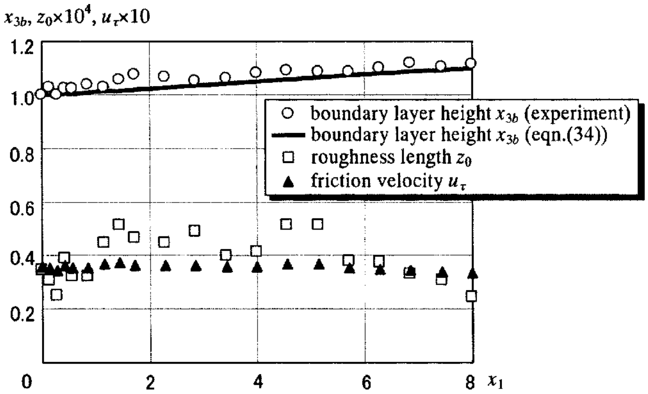

Fig. 4 Variation of boundary layer height, roughness length and friction velocity in x_1 direction

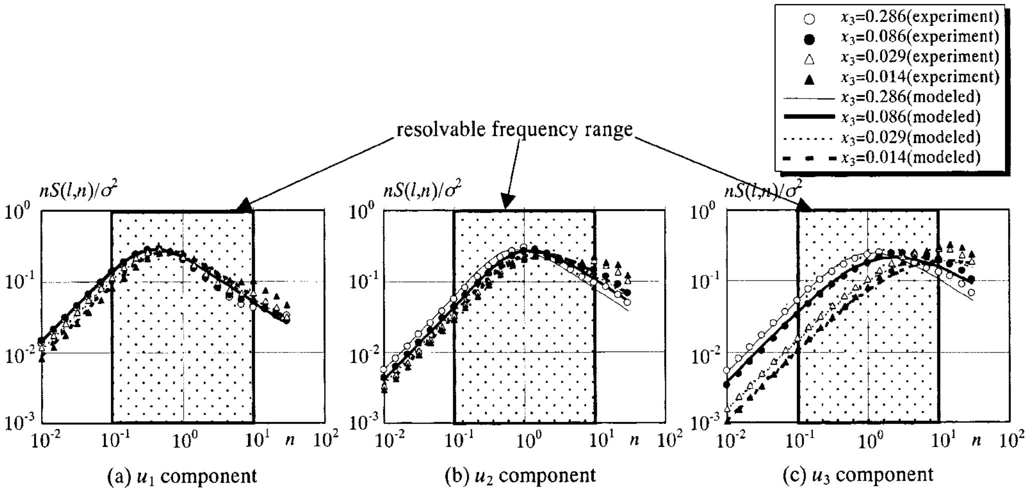

Fig. 5 Comparisons of power spectral densities ($x_1 = x_2 = 0$)

distribution of the velocity fluctuation is the same as the Gaussian distribution at every height. Fig. 4 shows the variation of boundary layer height, roughness length and friction velocity in the x_1 direction. The solid line in Fig. 5 indicates the boundary layer height calculated from the boundary layer equation in Appendix 1. The effect of growth of the boundary layer height was taken into consideration as the upper boundary condition.

3. Modeling of cross-spectral density matrix

Statistical characteristics of elements of the matrix, namely power spectral densities and cross-spectral densities, were investigated for modeling of the cross-spectral density matrix of the turbulent boundary layer. The model equations of power spectra and cross-spectra evaluated from the measured data are introduced here. The cross-spectra are modeled as root coherences and phase lags.

3.1. Model equations of power spectra

Fig. 5 shows the variation of the power spectra with the height x_3. The constraint effect of the wind tunnel floor is clearly observed in the power spectra near the floor and it is more evident in the power spectra of the u_3 component. The power spectra were modeled on the basis of a Kármán type spectrum giving priority to the degree of coincidence in the resolvable frequency range by LES using practical computation grids. The parameters for the model equations were modified to reproduce the influence of the floor by introducing the function of height in their expression.

$$\frac{S_{u1}(l,n)}{\sigma_{u1}^2(x_3)} = \frac{2\beta\lambda}{\{1+(cn\lambda)^\beta\}^{5/3\beta}} \tag{1}$$

$$\frac{S_{u2}(l,n)}{\sigma_{u2}^2(x_3)} = \frac{S_{u3}(l,n)}{\sigma_{u3}^2(x_3)} = \frac{\beta\lambda\{1+(8/3)(cn\lambda)^\beta\}}{\{1+(cn\lambda)^\beta\}^{(5/3\beta+1)}} \tag{2}$$

$$\begin{aligned} &\lambda = (2/\beta)L_{ui}(x_3)/\langle u_1(x_3)\rangle, \quad \beta = 2(x_3+A1)^{A2} \\ &c = 2\Gamma(1/\beta)\Gamma(2/3\beta)/\Gamma(5/3\beta), \; x_3 + A1 \le 1.0 \end{aligned} \tag{3}$$

Here, $S_{ui}(l,n)$: power spectrum of u_i at point l, $\sigma_{ui}(x_3)$: standard deviation of u_i at height x_3, $L_{ui}(x_3)$: turbulence scale of u_i obtained from test results of $S_{ui}(l,0)$ in Fig. 6, and Γ: gamma function, $A1$ and $A2$ in Table 1.

Fig. 5 compares the experimental and analytical model values of power spectra of the u_1, u_2, u_3 components at heights of $x_3 = 0.014$ to 0.286. The values coincide in the resolvable frequency range by LES.

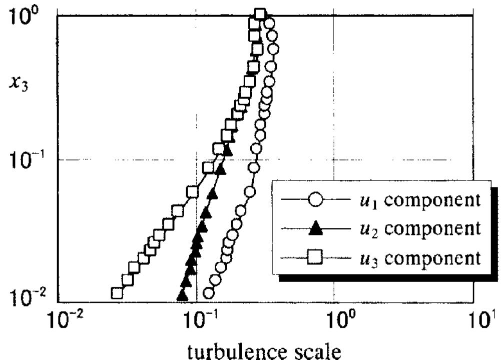

Fig. 6 Vertical profiles of turbulence scale of fluctuating wind velocities

Table 1 Coefficients for Eqs. (1)~(3)

Component	u_1	u_2	u_3
$A1$	0.0	0.0	0.1
$A2$	0.0	0.1	0.5

3.2. Model equations of root coherences and phase lags

Fig. 7 shows the variation of the root coherences and the phase lags in relation to the separation distance δx_3 of two points. The position of the reference point is fixed at $x_3 = 0.143$ in this case. If the absolute value of the distance δx_3 is the same, the characteristics of the root coherences and the phase lags vary depending on the position of the moving point. This is because of the constraint effect of the wind tunnel floor. The root coherences and phase lags were modeled by exponential-type and linear-type equations, respectively. The function of height was introduced into each model equation to reproduce the influence of the wind tunnel floor.

$$coh(l,p,n) = \{-B1|\delta x_{lp}| + (B2x_{3lp} + B3)\}\exp(-nF) \tag{4}$$

$$F = B4\{(|\delta x_{lp}| + B5)/x_{3lp}\}^{B6}(|\delta x_{lp}| + B5)/\langle u1(x_{3lp})\rangle \tag{5}$$

$$\begin{aligned}\phi(l,p,n) = {} & C1\{(|\delta x_{lp}| + C2)/x_{3lp}\}^{C3} n(|\delta x_{lp}| + C2) \\ & \cdot (\delta x_{lp}/|\delta x_{lp}|)/\langle u1(x_{3lp})\rangle + C4, \quad |\delta x_{lp}| \geq 0.03\end{aligned} \tag{6}$$

Here, $coh(l, p, n)$: root coherence between points l and p, ϕ (l, p, n): phase lag between points l and p, δx_{lp}: distance between points l and p, and x_{3lp}: mean height of points l and p, $B1$~$B6$ and $C1$~$C4$

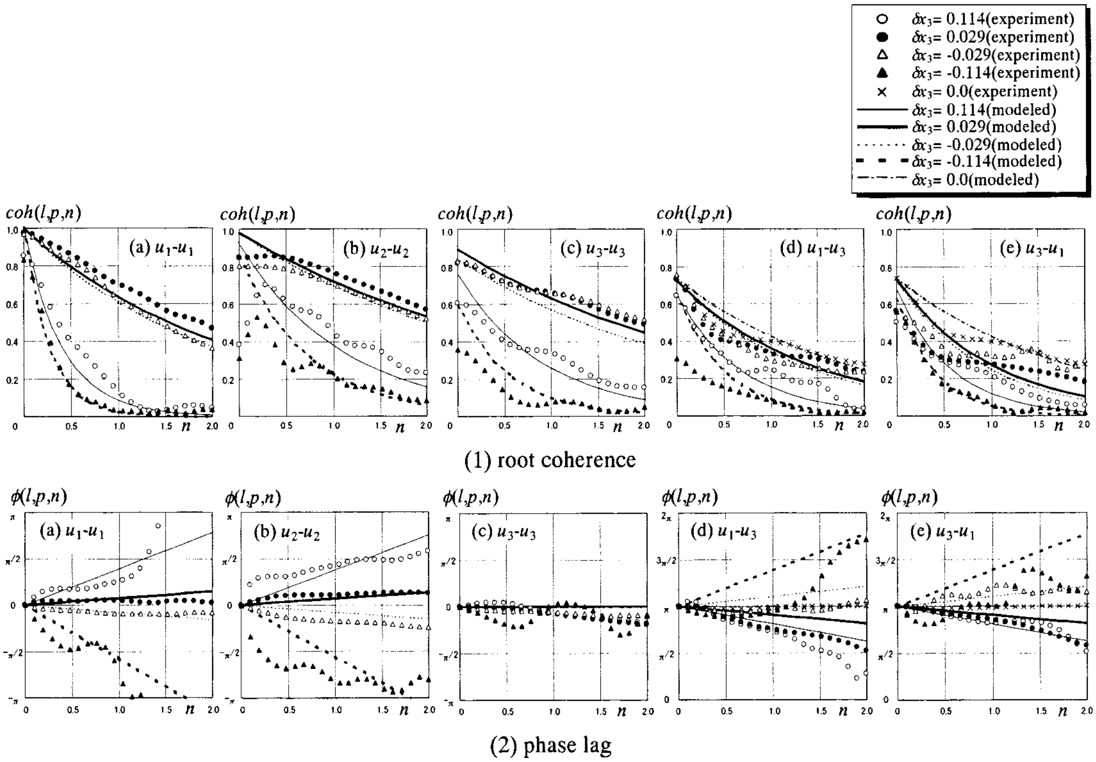

Fig. 7 Comparisons of root coherence and phase lag
(Reference point is fixed at $x_3 = 0.143$ and distance δx_3 between reference point and moving point is varied)

Table 2 Coefficients for Eqs. (4)~(12)

	u_1-u_1 vertical	u_2-u_2 vertical	u_3-u_3 vertical	u_1-u_3 vertical	u_3-u_1 vertical	u_1-u_1 horizontal	u_2-u_2 horizontal	u_3-u_3 horizontal	u_1-u_3 horizontal	u_3-u_1 horizontal	u_1-u_3 same point
$B1$	0.0	0.7	2.1	0.88	0.88	0.0	0.7	2.8	1.75	1.75	0.0
$B2$	0.0	1.75	1.75	0.0	0.5	0.0	1.17	3.06	5.25	5.25	5.0
$B3$	1.0	0.78	0.68	0.75	0.68	1.0	0.9	0.32	0.35	0.35	0.4
$B4$	18.0	5.0	6.0	6.0	6.0	18.0	6.0	7.0	8.0	8.0	$50x_3(\leq 7)$
$B5$	0.0	0.03	0.03	0.06	0.09	0.0	0.02	0.01	0.06	0.06	0.06
$B6$	0.3	0.3	0.4	0.2	0.2	0.3	0.5	0.3	0.1	0.1	0.05
$C1$	9.0	9.0	0.0	-2.0	-2.0	0.0	0.0	0.0	0.0	0.0	0.0
$C2$	0.0	0.0	0.0	0.09	0.09	-	-	-	-	-	-
$C3$	0.3	0.3	0.0	0.7	0.7	-	-	-	-	-	-
$C4$	0.0	0.0	0.0	π	π	0.0	0.0	0.0	π	π	π

in Table 2.

$B2x_{3lp} + B3 \leq 1.0$ (u_1-u_1, u_2-u_2, u_3-u_3 components)

$B2x_{3lp} + B3 \leq 0.8$ (u_1-u_3 component)

$B2x_{3lp} + B3 \leq 0.74$ (u_3-u_1 component)

$-B1|dx_{lp}| + (B2x_{3lp}+B3) \geq 0$

When two points align obliquely, the root coherence and the phase lag were modeled as per Eqs. (7)~(9).

$$coh(l, p, n) = D1 \exp(-n\sqrt{F_v^2 + F_h^2}) \tag{7}$$

$$D1 = -\sqrt{(B1_v|\delta x_{lp}|)^2 + (B1_h|\delta x_{lp}|)^2} + \{(B2_v x_{3lp} + B3_v) + (B2_h x_{3lp} + B3_h)\}/2 \tag{8}$$

$$\phi(l, p, n) = C1_v\{(|\delta x_3| + C2_v)/x_{3lp}\}^{C3v} n(|\delta x_3| + C2_v)(|\delta x_3|/\delta x_3)/\langle u_1(x_{3lp})\rangle + C4_v \tag{9}$$

Here, suffix v means vertical direction and h means horizontal direction.

$B2_v x_{3lp} + B3_v \leq 1.0$, $B2_h x_{3lp} + B3_h \leq 1.0$ (u_1-u_1, u_2-u_2, u_3-u_3 components)

$B2_v x_{3lp} + B3_v \leq 0.8$, $B2_h x_{3lp} + B3_h \leq 0.8$ (u_1-u_3 component)

$B2_v x_{3lp} + B3_v \leq 0.74$, $B2_h x_{3lp} + B3_h \leq 0.74$ (u_3-u_1 component), $D1 \geq 0$

At the same point, the root coherence and the phase lag were modeled as per Eqs. (10)~(12).

$$coh(l, p, n) = (B2x_3 + B3)\exp(-nF) \tag{10}$$

$$F = (B4x_3 + B5)(B6/x_3)^{B7} B6/\langle u_1(x_3)\rangle \tag{11}$$

$$\phi(l, p, n) = C4 \tag{12}$$

$$B2x_3 + B3 \leq 0.74,\ B4x_3 + B5 \leq 7.0$$

The cross-spectral density $S(l, p, n)$ between points l and p can be calculated from the power spectrum, the root coherence and the phase lag as per Eqs. (13)~(15).

$$S(l, p, n) = K(l, p, n) - iQ(l, p, n) \tag{13}$$

$$K(l, p, n) = coh(l, p, n)\sqrt{S(l, n)S(p, n)}\cos\phi(l, p, n) \tag{14}$$

$$Q(l, p, n) = coh(l, p, n)\sqrt{S(l, n)S(p, n)}\sin\phi(l, p, n) \tag{15}$$

Here, $S(l, p, n)$: cross-spectrum between points l and p, $K(l, p, n)$: co-spectrum between points l and p, and $Q(l, p, n)$: quadrature spectrum between points l and p.

Fig. 7 compares the experimental and analytical model root coherences and the phase lags. The model equations accurately express the experimental vales.

4. Method of generating inflow turbulence

The velocity fluctuation $u_i(l, t)$ at point l in the flowfield that satisfies the prescribed cross-spectral density matrix are expressed by Eqs. (16)~(19) using a trigonometric series with Gaussian random coefficients (Hoshiya 1972).

$$u_i(l, t) = \sum_{n=1}^{N}\sum_{p=1}^{l}[a_{lp}(\omega_n)\cos\{\omega_n t + \phi_{lp}(\omega_n)\} + b_{lp}(\omega_n)\sin\{\omega_n t + \phi_{lp}(\omega_n)\}] \tag{16}$$

$$\begin{aligned} a_{lp}(\omega_n) &= \sqrt{2\Delta\omega_n}\left|H_{lp}(\omega_n)\right|\xi_p(\omega_n) \\ b_{lp}(\omega_n) &= \sqrt{2\Delta\omega_n}\left|H_{lp}(\omega_n)\right|\eta_p(\omega_n) \end{aligned} \tag{17}$$

$$S(\omega_n) = H(\omega_n)H^{*T}(\omega_n) = \begin{bmatrix} H_{11}(\omega_n) & & \\ \vdots & \ddots & \\ H_{M1}(\omega_n) & \dots & H_{MM}(\omega_n) \end{bmatrix}\begin{bmatrix} H^*_{11}(\omega_n) & \dots & H^*_{M1}(\omega_n) \\ & \ddots & \vdots \\ & & H^*_{MM}(\omega_n) \end{bmatrix} \tag{18}$$

$$\phi_{lp}(\omega_n) = \tan^{-1}\{-I_m H_{lp}(\omega_n)/R_e H_{lp}(\omega_n)\} \tag{19}$$

Here, i : direction of spatial coordinate ($i = 1$ streamwise, $i = 2$ lateral, $i = 3$ vertical),

l, p : indices denoting two points related to cross-spectral density $H_{lp}(\omega_n)$ at points l and p ($l = 1, \cdots, M$, $p = 1, \cdots, l$),

M : total number of nodal points in the region where inflow turbulence was generated simultaneously,

N : total number of frequency intervals,

ω_n	:	circular frequency,
$\Delta\omega_n$	:	interval of circular frequency,
$a_{lp}(\omega_n)$, $b_{lp}(\omega_n)$	:	Fourier coefficients,
$\phi_{lp}(\omega_n)$	:	phase lag,
$\xi_{lp}(\omega_n)$, $\eta_{lp}(\omega_n)$	:	independent Gaussian random number with mean value 0 and standard deviation 1,
$S(\omega_n)$	:	cross-spectral density matrix,
$H(\omega_n)$	:	lower triangular matrix of $S(\omega_n)$,
$H_{lp}(\omega_n)$	:	component of $H(\omega_n)$,

*:conjugate, Re : real part, Im : imaginary part

5. LES computation of turbulent boundary layer developed over flat plate

We investigated how the degree of correspondence of the cross-spectral density matrix of the generated inflow turbulence with the target cross-spectral density matrix influenced the LES results for the turbulent boundary layer. Several types of inflow turbulence were generated considering several reproduction levels of cross-spectral density matrices (cf. Table 3).

LES computations were conducted by imposing these types of inflow turbulence on their inflow

Table 3 Reproduced cross-spectral matrix components for inflow turbulence generation

Case	Power spectrum	Cross-spectrum
1	white noise	not reproduced
2	u_1, u_2, u_3 component	not reproduced
3	u_1, u_2, u_3 component	u_1-u_1, u_2-u_2, u_3-u_3 component (shear component is not reproduced)
4	u_1, u_2, u_3 component	u_1-u_1, u_2-u_2, u_3-u_3, u_1-u_3 component

Table 4 Boundary condition of LES

inflow	generated inflow turbulence
outflow	convective boundary condition (Dai, Kobayashi and Taniguchi 1994) $\dfrac{\partial u_i}{\partial t} + U_c \dfrac{\partial u_i}{\partial x_1} = 0$ U_c : convective velocity (value of u_1 component averaged over inflow boundary plane)
floor	linear-power law type wall function (Werner and Wengle 1991)
upper	$\overline{u_1}$, $\overline{u_2}$ components : $\partial\langle\overline{u_1}\rangle/\partial x_3 = 0$, $\partial\langle\overline{u_2}\rangle/\partial x_3 = 0$ $\overline{u_3}$ component : $\langle\overline{u_3(x_1)}\rangle = U_b(\partial\delta^*/\partial x_1)$ δ^* : displacement thickness (Appendix 1) U_b : $\overline{u_1}$ at boundary layer height $\langle f \rangle$: time aberaged value, f : filtered value
side	periodic boundary condition

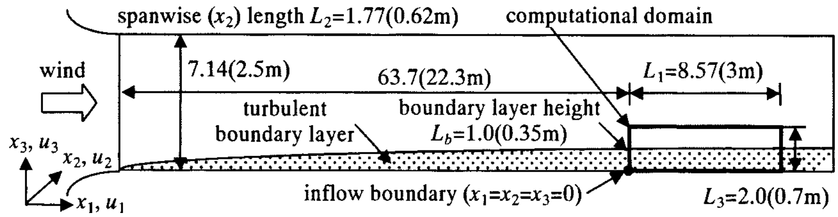

Fig. 8 Outline of turbulent boundary layer and computational domain

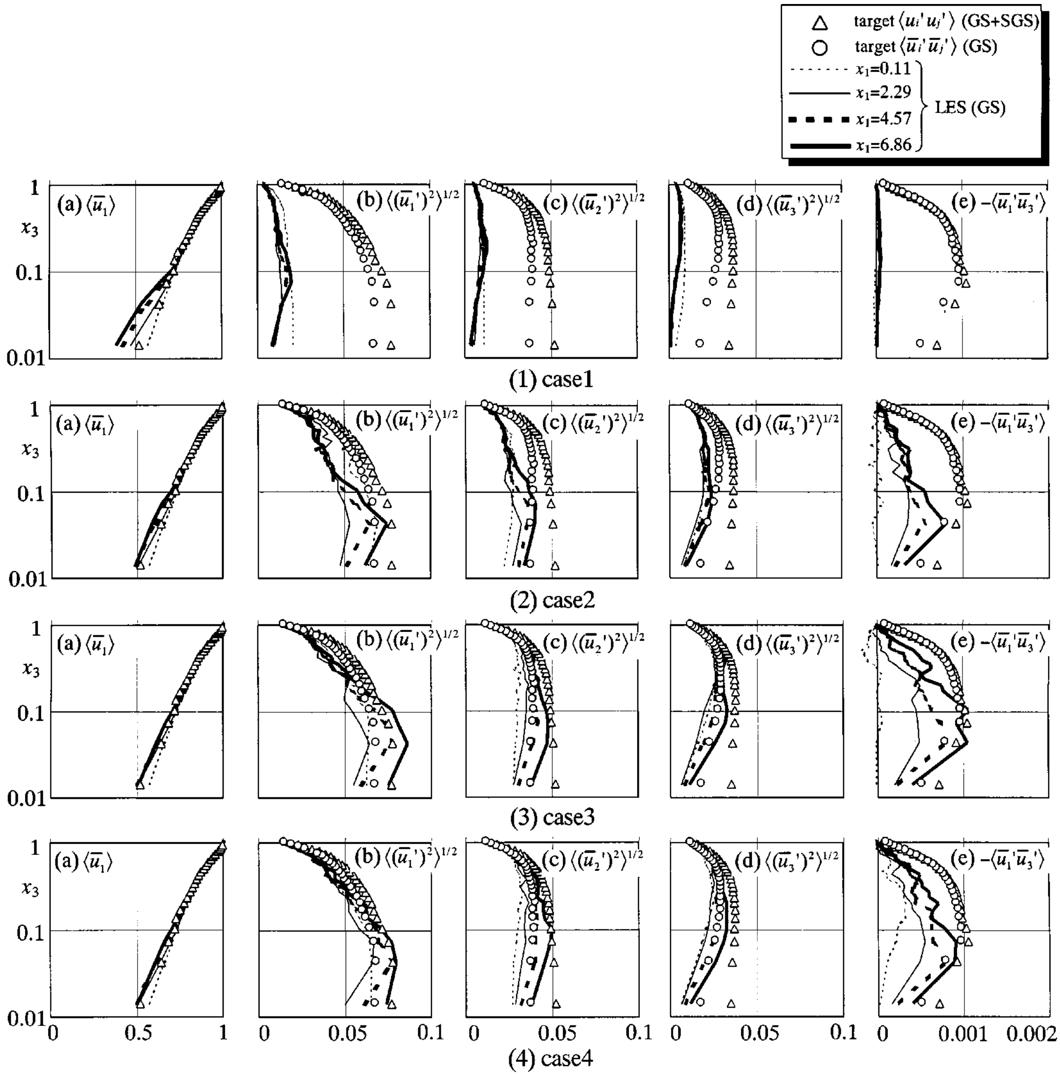

Fig. 9 Comparisons of mean and fluctuating velocity profiles

boundary. The Smagorinsky model (C_S = 0.1) was used for LES. A second order centered difference scheme was adopted for spatial derivatives. In the time advancement, the Adams-Bashforth scheme was used for the convection terms and the Crank-Nicolson scheme was used for the diffusion terms. The time icrement was Δt = 0.00829 and the total number of computation steps was 8200. The boundary condition of LES is shown in Table 4. The computational domain covered $8.57(x_1) \times 1.77(x_2) \times 2.0(x_3)$. This computational domain was discretized into $150(x_1) \times 31(x_2) \times 42(x_3)$ grids. A staggered grid arrangement was employed. Fig. 8 outlines the turbulent boundary layer and the computational domain.

Fig. 9 compares mean and fluctuating wind velocity profiles between the target values of inflow turbulence generation and the grid scale (GS) components of LES results estimated considering the grid filter effect of LES. Results of case 1 could not reproduce either the target values of mean or fluctuating velocities at any positions in the computational domain. Although the mean and fluctuating velocities changed from the target values in the region of x_1 = 0.11~2.29 in case 2, the changes were smaller than those in case 1. However, a relatively large transition of the normal component $\langle (\bar{u}_1')^2 \rangle^{1/2}$ was observed at x_1 = 0.11~2.29. Furthermore, the development of the shear component $-\langle \bar{u}_1' \bar{u}_3' \rangle$ was slower than those for cases 3 and 4. For case 3, the transition of mean and fluctuating velocities near the inflow boundary and the development of shear components were improved from those for case 2. The differences between the results for case 3 and case 4 were small with regard to the mean and normal components. The shear component at x_1 = 0.11 for case 4 was better than that for case 3. However, the shear components in both case 3 and case 4 were quickly recovered in the region of x_1 = 0.11~2.29, and no differences were observed in other regions between these two cases. The target turbulence quantities of grid scale components were reproduced well for cases 3 and 4.

Here, we discuss the reason for this quick recovery of the fluctuating wind velocities and the shear stress. The production term P_k of the transport equation of turbulence kinetic energy k can expressed as Eq. (22).

$$P_k = -\langle \bar{u}_i' \bar{u}_k' \rangle \frac{\partial \langle \bar{u}_i \rangle}{\partial x_k} \tag{22}$$

The production term P_{ij} of the transport equation of shear stress $-\langle \bar{u}_i' \bar{u}_j' \rangle$ can expressed as Eq. (23).

$$P_{ij} = -\langle \bar{u}_i' \bar{u}_k' \rangle \frac{\partial \langle \bar{u}_j \rangle}{\partial x_k} - \langle \bar{u}_j' \bar{u}_k' \rangle \frac{\partial \langle \bar{u}_i \rangle}{\partial x_k} \tag{23}$$

Furthermore, Eq. (24) can be obtained for a well developed turbulent boundary layer.

$$\langle \bar{u}_2 \rangle = \langle \bar{u}_3 \rangle \approx 0, \quad -\langle \bar{u}_1' \bar{u}_2' \rangle = -\langle \bar{u}_2' \bar{u}_3' \rangle \approx 0, \quad \frac{\partial \langle f \rangle}{\partial x_1} = \frac{\partial \langle f \rangle}{\partial x_2} \approx 0 \tag{24}$$

The production term P_k of the turbulence kinetic energy k and the production term P_{13} of the transportation equation of the shear stress $-\langle \bar{u}_1' \bar{u}_3' \rangle$ can be derived from these Eqs. (22)~(24) as follows.

$$P_k = -\langle \bar{u}_1' \bar{u}_3' \rangle \frac{\partial \langle \bar{u}_1 \rangle}{\partial x_3} \tag{25}$$

$$P_{13} = -\langle (\bar{u}_3')^2 \rangle \frac{\partial \langle \bar{u}_1 \rangle}{\partial x_3} \tag{26}$$

Eq. (25) indicates that the turbulence kinetic energy k can be produced correctly if the gradient of the vertical profile of mean velocity $\langle \overline{u_1} \rangle$ and the shear stress $-\langle \overline{u_1' u_3'} \rangle$ are reproduced. Eq. (26) means that the shear stress $-\langle \overline{u_1' u_3'} \rangle$, which contributes to the production of k, can be produced correctly if the vertical gradient of $\langle \overline{u_1} \rangle$ and the fluctuating velocity $\langle \overline{(u_3')^2} \rangle^{1/2}$ are reproduced well. Therefore, if we simulate the vertical gradient of $\langle \overline{u_1'} \rangle$ and the fluctuating velocity $\langle \overline{(u_3')^2} \rangle^{1/2}$ in the inflow turbulence generation, the fluctuating velocities $\langle \overline{(u_1')^2} \rangle^{1/2}$, $\langle \overline{(u_2')^2} \rangle^{1/2}$, $\langle \overline{(u_3')^2} \rangle^{1/2}$ and the shear stress $-\langle \overline{u_1' u_3'} \rangle$ can be reproduced within a certain degree. These conditions were satisfied for cases 1 to 4. For case 1, however, since the fluctuating velocity $\langle \overline{(u_3')^2} \rangle^{1/2}$ greatly decreased just behind the inflow boundary due to the fliter effect of LES computation, the productions of k and $-\langle \overline{u_1' u_3'} \rangle$ were very small and $\langle \overline{(u_1')^2} \rangle^{1/2}$, $\langle \overline{(u_2')^2} \rangle^{1/2}$, $\langle \overline{(u_3')^2} \rangle^{1/2}$ and $-\langle \overline{u_1' u_3'} \rangle$ did not recover at all in the downstream region. For case 2, which did not reproduce the spatial correlation, since the fluctuating velocity $\langle \overline{(u_3')^2} \rangle^{1/2}$ was smaller than those for cases 3 and 4, the recovery of fluctuating velocities and $-\langle \overline{u_1' u_3'} \rangle$ was slower.

Fig. 10 compares power spectra of the u_1 and u_3 components. For each case, the power spectra of the inflow turbulence agreed well with the target values. There was almost no transition between the

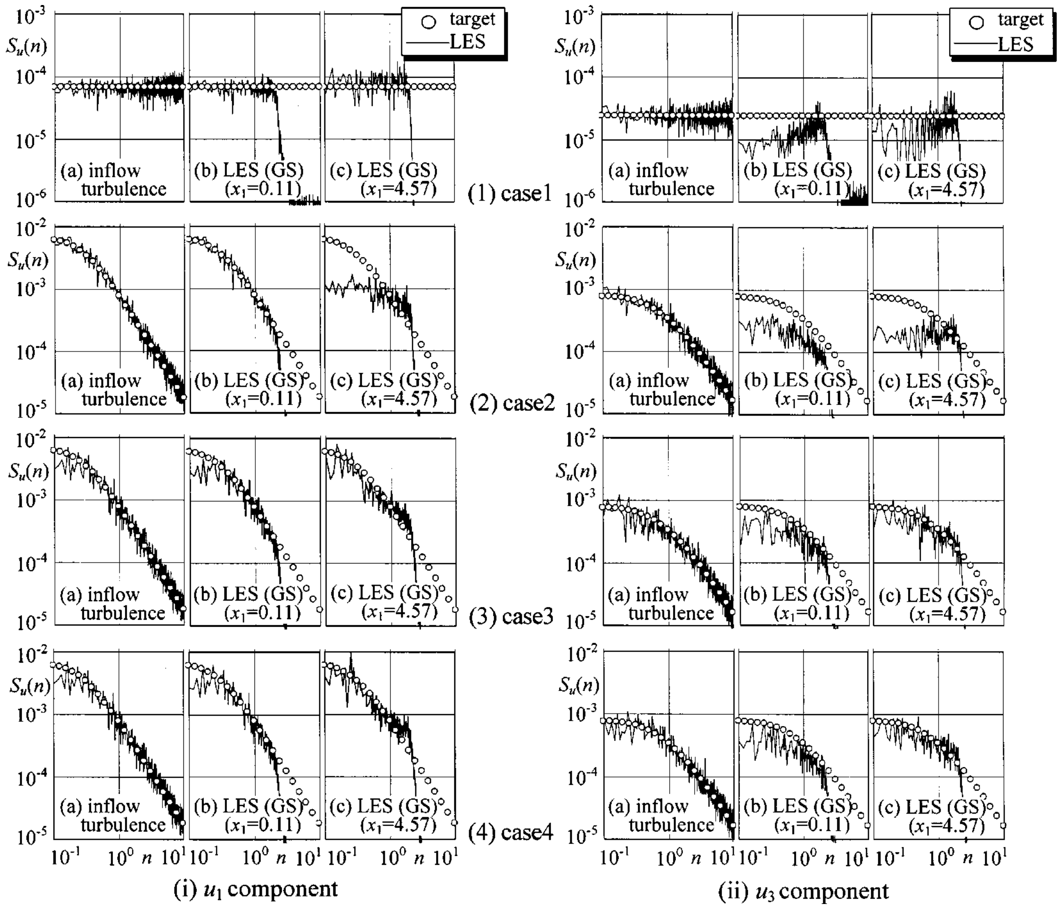

Fig. 10 Comparisons of power spectra (x_3 = 0.2)

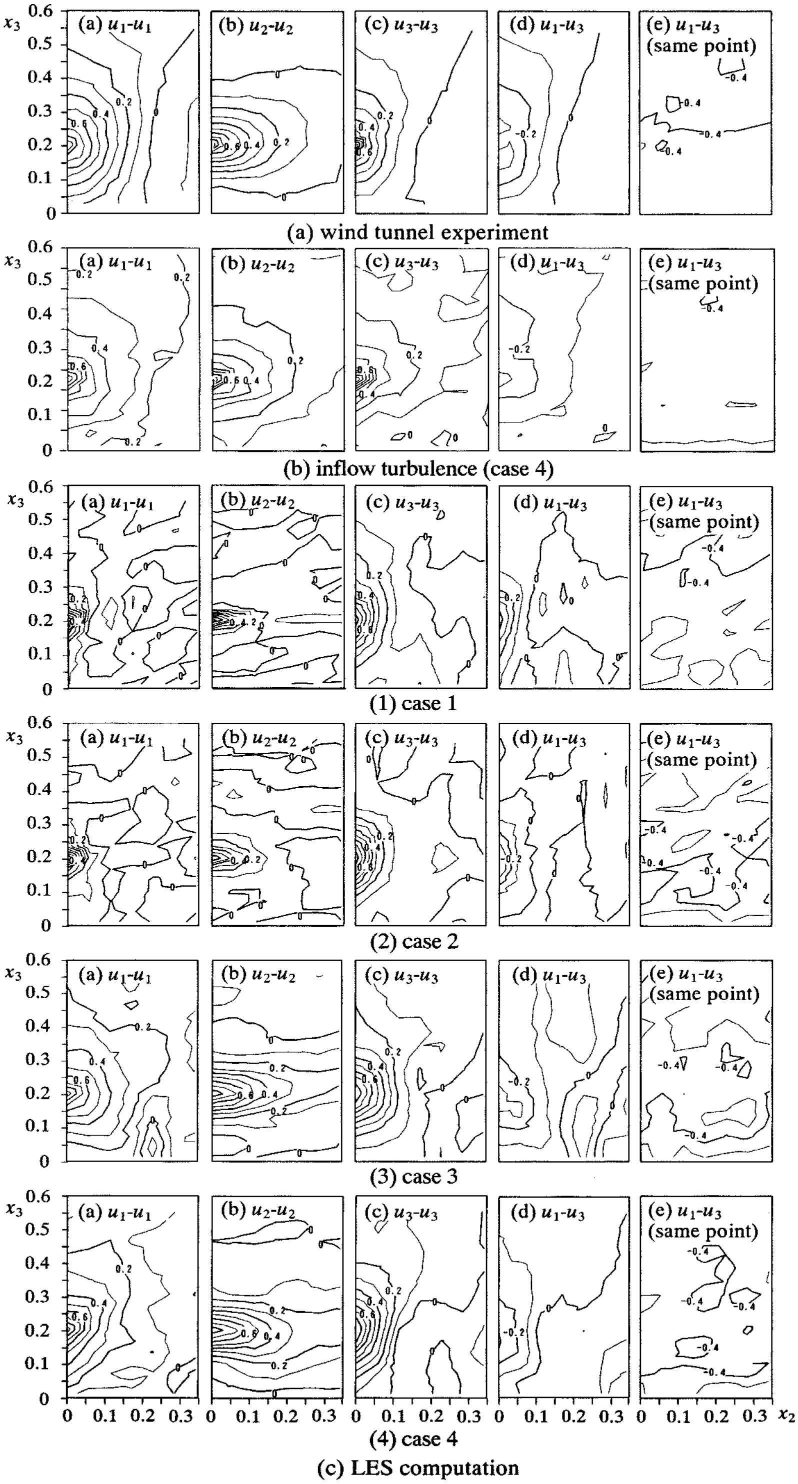

Fig. 11 Comparisons of spatial correlation (reference point : $x_1 = 4.57$, $x_2 = 0$, $x_3 = 0.2$)

power spectra of the u_1 component at $x_1 = 0.11$ and those of the inflow turbulence, except the grid filter effect of LES computation. The power spectra of the u_3 component at $x_1 = 0.11$ were less than those of the inflow turbulence caused by the filter effect of the spatial interpolation of the inflow

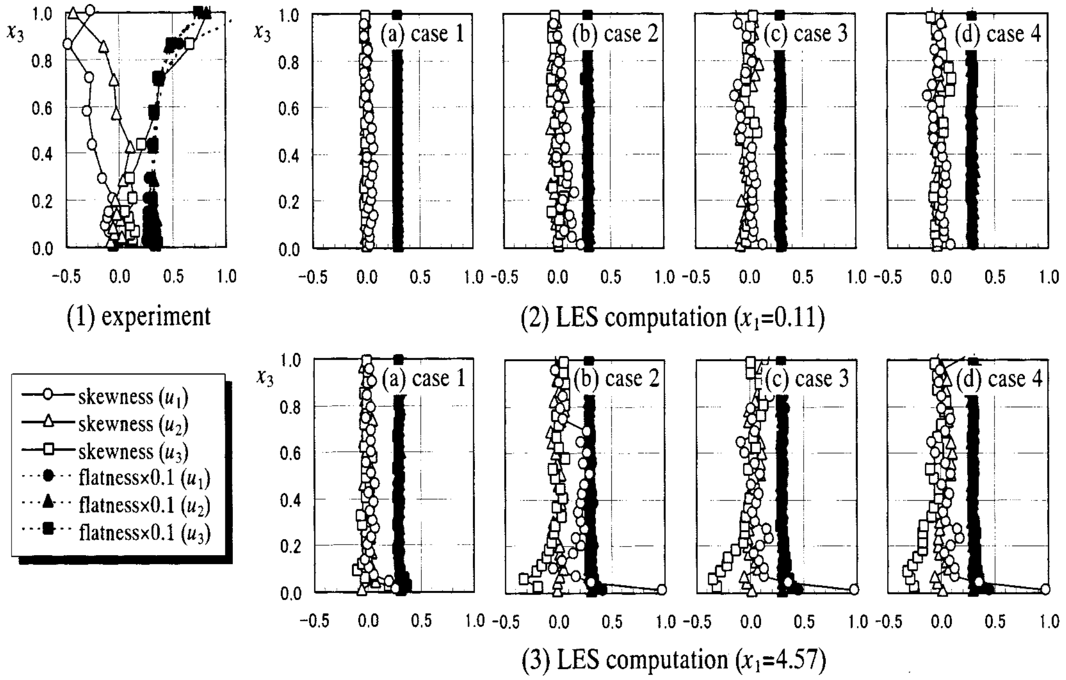

Fig. 12 Comparisons of frequency distribution of velocity fluctuation

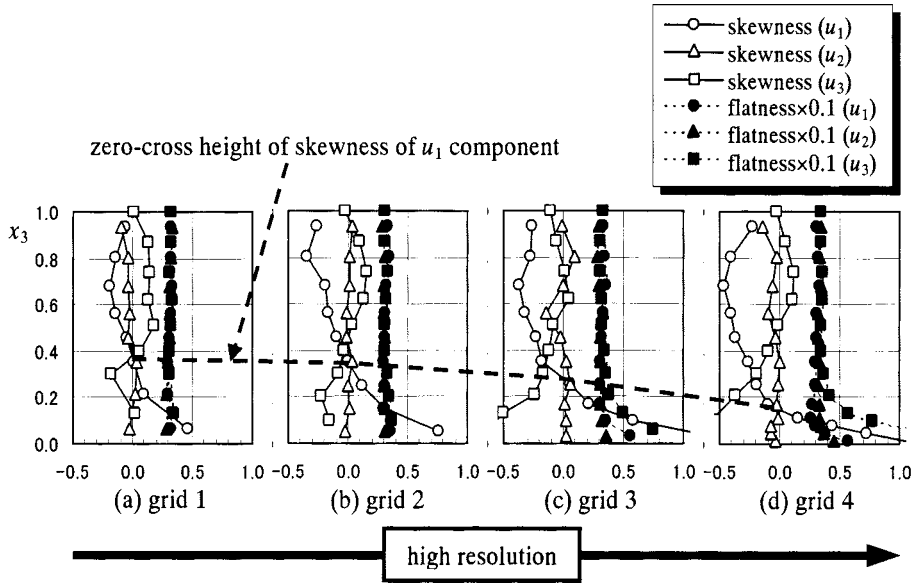

Fig. 13 Variation of frequency distribution of velocity fluctuation in channel flow with grid resolution

turbulence and the decreasing effect during the process in which the inflow turbulence adapted itself to the discretized N-S equations and the continuity equation. However, evident differences can be observed between the values for case 1 and case 2, and those for case 3 and case 4 at $x_1 = 4.57$. The power spectra of LES results coincided closely with the target values for cases 3 and 4, but the values for case 2 resembled those for case 1.

Fig. 11 compares the spatial correlations at $x_1 = 4.57$. For the inflow turbulence, only the result for case 4 is displayed. The spatial correlations of generated inflow turbulence for case 4, which reproduced not only the power spectra but also the cross-spectra of normal components and shear component, show good agreement with the experimental results. The spatial correlations of LES computation for case 3 and case 4 can reproduce the experimental results for each component. However, the reproduciability of the spatial correlations for case 1 or case 2 is not enough at $x_1 = 4.57$.

Fig. 12 compares the frequencey distributions of wind velocity fluctuations. The skewness and flatness do not change from the Gaussian distribution, which was adopted in the inflow turbulence generation, just behind the inflow boundary ($x_1 = 0.11$) for each case. In the downstream region ($x_1 = 4.57$), the constraint effect of the wind tunnel floor is clearly observed in the skewness of the u_1 and u_3 components at $x_3 \leq 0.1$. However, this effect is not so evident in the distribution of flatness.

To confirm this variation of skewness, LES computation of a channel flow was conducted using several grid resolutions. The length scale and the time scale were normalized by the half height δ of the channel width and the mean velocity U_c at the center of the channel. The Reynolds number was $R_e = U_c\delta / \nu = 13800$. The computational domain covered $2\pi(x_1)\times \pi(x_2)\times 2(x_3)$. The grid arrangement is shown in Appendix 2.

Fig. 13 compares of the variation of frequency distribution in the channel flow with grid resolution. The finer the grid resolution used, the larger the change of skewness of u_1 and u_3 components near the wall surface appeared. Furthermore, the coarser the grid resolution used, the higher the zero-cross height of skewness of the u_1 component. Thus, the reason that the frequency distributions of velocity fluctuations of the turbulent boundary layer computed by LES was different from those of the experimental results near the floor surface was supposed to be caused by the relatively coarse grid resolution in this region.

6. Conclusions

When an inflow turbulence was generated considering only the power spectra of each velocity vector component as the target (case 2), power spectra, spatial correlation and velocity profiles could not be reproduced in LES using the generated inflow turbulence. The target turbulence quantities of grid scale components were reproduced well, where the cross-spectra of the normal components were considered in addition to the power spectra as the target in the generation procedure (case 3). Therefore, reproduction of the cross-spectra of the normal components in the inflow turbulence generation was very important for reproducing those turbulence quantities in LES. Case 4 considered the cross-spectra of the shear component in addition to those of the normal components. In the result of this case, it was clarified that the spatial correlation of the shear component just behind the inflow boundary was more reproducible than that in case 3. However, there were no differences in other regions between the results for case 3 and case 4, and the target turbulence quantities of the grid scale components were reproduced well for each case. Since this method can reproduce various kinds of flowfield that cannot be reproduced by CFD methods, it is expected to become a very useful tool for investigating interaction between flowfields around structures and pressure distributions on their surfaces.

Appendix 1

The boundary layer equation of the turbulent boundary layer is expressed as Eq. (27).

$$\frac{d}{dx_1}(\rho U_b^2 \theta) = \frac{dP}{dx_1}\delta^* + \tau_0 \tag{27}$$

To substitute Eq. (27) for Eqs. (28)~(33) on condition of $dP/dx_1 = 0$, the boundary layer height δ and the displacement thickness δ^* can be obtained as Eqs. (34)~(36).

$$d^* = \int_0^\delta (1 - \langle u_1 \rangle) dx_3 \tag{28}$$

$$\theta = \int_0^\delta (1 - \langle u_1 \rangle)\langle u_1 \rangle dx_3 \tag{29}$$

$$\langle u_1 \rangle = (x_3/\delta)^{1/7} \tag{30}$$

$$\tau_0 = \psi_1 \rho U_b^2 / 2 \tag{31}$$

$$\psi_1 = 0.0593 R_\delta^{-1/4} \tag{32}$$

$$R_\delta = U_b \delta / \nu \tag{33}$$

$$\delta = 0.462 R_e^{-1/5} (x_1 + 63.7)^{4/5} \tag{34}$$

$$\delta^* = \delta / 8 \tag{35}$$

$$R_e = U_b L_b / \nu \tag{36}$$

Here, ρ : air density, θ : momentum thickness, δ^* : displacement thickness, τ_0 : shear stress, P : pressure, ψ_1 : drag coefficient, and R_δ : Reynolds stress defined by δ, U_b.

In these formula, it is assumed that the turbulent boundary layer developed from $x_1 = -63.7$.

Appendix 2

The computational domain was discretized into $26(x_1) \times 26(x_2)$ with equi-spaced grids in the x_1 and x_2 directions. In the x_3 direction, four types of grid resolution were examined near the wall surfaces (at $x_3 = 0$~0.3 and 1.7~2.0). The following parentheses indicate the grid spacings δx_3 near the wall surfaces for each case. The same grid arrangement was used at $x_3 = 0.3$~1.7.

(a) grid 1 : number of nodal point is 18 in the x_3 direction ($\delta x_3 = 0.13$, 0.17)
(b) grid 2 : number of nodal point is 20 in the x_3 direction ($\delta x_3 = 0.10$, 0.10, 0.10)
(c) grid 3 : number of nodal point is 22 in the x_3 direction ($\delta x_3 = 0.06$, 0.07, 0.08, 0.09)
(d) grid 4 : number of nodal point is 26 in the x_3 direction ($\delta x_3 = 0.03$, 0.03, 0.035, 0.035, 0.08, 0.09)

A staggered grid arrangement was employed. The periodic boundary condition was utilized for the inflow, outflow and side wall boundary conditions. The linear-power law type wall function (Werner-Wengle 1991) was used for the floor boundary condition. The Smagorinsky model ($Cs = 0.1$) was utilized for the SGS model, the time increment was $\Delta t = 0.001$ and the total number of computation steps was about 16400.

References

Dai, T., Kobayashi, T. and Taniguchi, N. (1994), "Large eddy simulation of plane turbulent jet flow using a new outflow velocity boundary condition", *JSME Int. Journal*, Series B, **37**(2), 242-253.

Hoshiya, M. (1972), "Simulation of multi-correlated random processes and application to structural vibration problems", *Proc. of JSCE*, No.204, 121-128.

Iizuka, S., Murakami, S., Tsuchiya, N. and Mochida, A. (1999), "LES of flow past 2D cylinder with imposed inflow turbulence", *Proc. 10th Int. Conf. Wind Eng.*, **2**, 1291-1298.

Kondo, K., Mochida, A. and Murakami, S. (1997), "Generation of velocity fluctuations for inflow boundary condition of LES", *J. Wind Eng. Ind. Aerod.*, **67 & 68**, 51-64.

Lund, T.S., Wu, X. and Squires, K.D. (1998), "Generation of turbulent inflow data for spatially-developing boundary layer similations", *J. Computational Physics*, No. 140, 233-258.

Maruyama, T., Rodi, W., Maruyama, Y. and Hiraoka, H. (1999), "Large eddy simulation of the turbulent boundary layer behind roughness elements using an artificially generated inflow", *J. Wind Eng. Ind. Aerod.*, **83**, 381-392.

Werner, H. and Wengle, H. (1991), "Large eddy simulation of turbulent flow over and around a cube in plane channel", *Proc. 8th Symp. on Turbulent Shear Flows*, 19-4.